Progress In Electromagnetics Research B, Vol. 54, 107–128, 2013

AN IMPROVED SAR RADIOMETRIC TERRAIN CORRECTION METHOD AND ITS APPLICATION IN POLARIMETRIC SAR TERRAIN EFFECT REDUCTION

Peng Wang [1, 2, *], Qin Ma [3], Jinfei Wang [3], Wen Hong [1], Yang Li [1], and Zhaohua Chen [3]

[1]Science and Technology on Microwave Imaging Laboratory, Institute of Electronics, Chinese Academy of Sciences, Beijing 100190, China

[2]University of Chinese Academy of Sciences, Beijing 100190, China

[3]Department of Geography, The University of Western Ontario, London, Ontario N6A 5C2, Canada

Abstract—A new SAR radiometric terrain correction method was proposed to reduce the terrain effects in sloped regions. Based on this method, a procedure for polarimetric SAR terrain effect reduction was proposed, including geometric correction, shadow detection, radiometric terrain correction, and polarization orientation angle shift compensation. Experiments using RADARSAT-2 polarimetric SAR data of the Three Gorges Area, China demonstrated the effectiveness of the proposed radiometric terrain correction method. Both visual and quantitative analyses showed that after the proposed radiometric terrain correction method was applied, the contrast between different slopes that caused by local incidence angle differences, foreshortening, and layover was significantly reduced. The difference of backscattering intensity on slopes facing the radar sensor and facing away from the sensor was reduced from 12.5 dB before radiometric correction to 1.3 dB. The overall accuracy of land use/land cover classification was improved by 11.2 percent using the terrain corrected polarimetric SAR data.

Received 20 May 2013, Accepted 21 August 2013, Scheduled 29 August 2013

* Corresponding author: Peng Wang (wangpeng84sl@gmail.com).

1. INTRODUCTION

Applications of polarimetric synthetic aperture radar (SAR) for remote sensing have expanded rapidly during the last two decades due to the abundant availability of airborne and space-borne polarimetric SAR data. These applications include land use/land cover mapping [1–9], change detection, hazard monitoring and damage assessment, surface geophysical parameters retrieval [10], biomass and forest height estimation, etc. [11]. Algorithms based on the backscattering intensity of different polarization channels and various polarimetric target decomposition parameters were developed for those applications. Most of them perform well in flat regions. However, when it comes to sloped regions, distortions in SAR images occur: (1) Geometric distortion. Because the cross-track dimension in SAR image is determined by a time measurement associated with the slant range from the sensor to the target, SAR images present inherent geometrical distortions that due to the difference between the slant range and the ground range [11]. Moreover, in high relief regions, foreshortening and even layover may occur due to the unproportioned relationship between the slant range and ground range. This cannot be rectified using polynomial transformation. (2) Radiometric distortion. Radar backscatter brightness varies with topographic slopes with different local incidence angles. Besides, in foreshortening and layover regions, the backscatter from more than one ground element might overlap on one image pixel, thus the backscattering power accumulates correspondingly. (3) Polarization states distortion. The azimuth slope causes polarization orientation angle (POA) shift, thus causes rotation of the polarimetric backscattering matrix [11–14].

These terrain effect induced distortions need to be corrected before polarimetric SAR applications. Efforts have been dedicated to correct each of them. For correction of geometric distortions, the traditional geometric correction method through polynomial transformation does not work in finding out the corresponding relationship of coordinates between the SAR image coordinates and the real world coordinates. According to [15–17], the range direction coordinate in SAR image is determined by the slant range, while the azimuth direction coordinate can be calculated by solving the zero-Doppler shift equation. Chen [18] adopted another geometric correction method using SAR simulation [19, 20] and registration. For the radiometric distortions, earlier algorithms tried to perform the correction based on local incidence angle [21, 22] or surface tilt angles [23, 24]. Ulander [25] proposed a radiometric slope correction method based on the angle between the slope surface and the image

plane, and proved that the former correction algorithms that based on local incidence angles or surface tilt angles were approximations to his correction method. Tilley and Bonwit [26] and Bolter et al. [27] proposed to normalize the brightness values of SAR image pixels in foreshortening and layover areas by dividing the value equally among all ground patches contributing to that particular SAR pixel. Small et al. [17, 28] proposed a correction method by normalizing the backscatter coefficient with the local illuminated area projected onto the plane perpendicular to the radar line of sight. For polarization distortion, researchers proposed to perform the correction through polarization orientation angle shift compensation [12–14, 29]. The effects of polarization orientation angle shift compensation on polarimetric SAR data have been studied [14, 29, 30].

There have been very few papers published about applying radiometric terrain correction on polarimetric SAR data. In this study, a new radiometric terrain correction method was proposed and compared with other radiometric terrain correction methods. Based on the new radiometric terrain correction method, a procedure for polarimetric SAR terrain effect correction that combines geometric terrain correction, radiometric terrain correction, and polarization orientation angle shift compensation was proposed.

2. METHODOLOGY

2.1. SAR Geometric Terrain Correction

One important step for SAR geometric correction is to find the relationship between real world coordinates and the corresponding coordinates in a SAR image. In sloped regions, due to the special characteristics of SAR imaging, this cannot be achieved by selecting ground control points and applying polynomial transformation. Generally, a DEM (digital elevation model) is needed to accomplish SAR geometric correction. Since a SAR image is a range-Doppler image, for each DEM cell, the corresponding coordinate in the range direction can be calculated through the slant range between the DEM cell and radar sensor, while the coordinate in the azimuth direction can be obtained by finding out the corresponding zero-Doppler frequency shift position. Details can be found in the papers by Loew and Mauser [16], Meier et al. [15], and Small [17].

2.2. SAR Radiometric Terrain Correction

Radar backscatter β is defined as the ratio of scattered power P_S to the incident power P_I [17]. For distributed targets, radar brightness β^0 is

defined as averaged backscatter ratio per unit area in the image plane (i.e., the slant range plane) [31]; backscatter coefficient σ^0 is defined as averaged backscatter ratio per unit ground area. For flat areas, the backscatter coefficient σ^0 can be retrieved using [17] incident angle θ

$$\sigma^0 = \beta^0 \cdot \sin\theta \tag{1}$$

In sloped regions, there are radiometric distortions in the backscatter coefficient retrieved using (1), since σ^0 depends on the local scattering geometry. To minimize the radiometric distortions caused by topographic effects, backscatter coefficient parameter that is less affected by terrain slopes need to be retrieved.

Assume that N slope surface patches S_i ($i = 1, 2, \ldots, N$) (see Figure 1) with the same slant range R_S to the SAR sensor are projected into the same pixel O in the SAR image (Assume that the ground surface is divided into very small pieces, thus each pixel in the SAR image contains the backscatter contribution from more than one ground patches). The corresponding areas of these ground surface patches are A_i ($i = 1, 2, \ldots, N$), while their projected areas onto the gamma plane (i.e., the plane perpendicular to radar line of sight) are B_i ($i = 1, 2, \ldots, N$). Q is the incident power density (i.e., power per unit area) on the surface of gamma plane with slant range R_S to the SAR sensor. Therefore, the incident power on surface patch S_i is $P_{Ii} = Q \cdot B_i$; thus the scattered power of surface patch S_i is

$$P_{Si} = P_{Ii} \cdot \sigma_i = Q \cdot B_i \cdot \sigma_i^0 \cdot A_i \tag{2}$$

where $\sigma_i = \sigma_i^0 \cdot A_i$ is the backscatter ratio of surface patch S_i. The

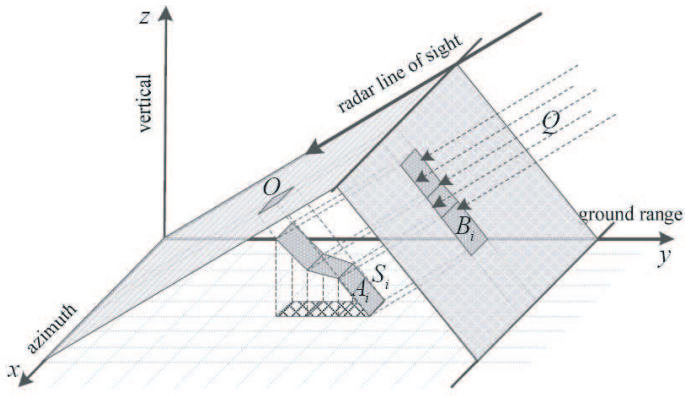

Figure 1. Geometry of a slope surface patch S_i and its projection on the image plane and the gamma plane.

total scattered power from these N patches $P_S = \sum_{i=1}^{N} P_{Si}$ is projected onto the SAR image pixel O. For pixel O, the radar brightness β^0 can be obtained by [17]

$$\beta^0 = \frac{\beta}{A_\beta} = \frac{P_S/P_I}{A_\beta} \tag{3}$$

where A_β is the reference area on the radar image plane, i.e., the image pixel size. The area in the gamma plane corresponding to each pixel of the SAR image is $A_\beta \tan^{-1}\theta$, thus the incident power corresponding to each pixel is

$$P_I = Q \cdot A_\beta \tan^{-1}\theta \tag{4}$$

From (2), (3) and (4),

$$\beta^0 \cdot A_\beta^2 \cdot \tan^{-1}\theta = \sum_{i=1}^{N} B_i \cdot \sigma_i^0 \cdot A_i \tag{5}$$

Since (5) is an underdetermined equation, proper assumptions have to be made to solve the equation. Assume that the N patches have the same backscatter coefficients $\sigma_i^0 = \sigma_T^0$, thus

$$\sigma_T^0 = \beta^0 \cdot \frac{A_\beta^2 \cdot \tan^{-1}\theta}{\sum_{i=1}^{N} B_i \cdot A_i} \tag{6}$$

For polarimetric SAR radiometric correction, the backscatter coefficient is proportional to $|S_{pq}|^2$ [11], $(p, q = H, V)$, the polarimetric backscattering matrix can be corrected using

$$S_2' = S_2 \cdot \sqrt{\frac{A_\beta^2 \cdot \tan^{-1}\theta}{\sum_{i=1}^{N} B_i \cdot A_i}} \tag{7}$$

To accomplish this radiometric correction method, a simulated SAR image of the denominator of (6) is created first, using corresponding DEM data. The DEM grid cell should be small enough, so that each SAR image pixel relates to more than one DEM patches. Therefore, a fine spatial resolution DEM data is needed. If the obtained DEM data has coarse spatial resolution, it must be resampled to higher resolution. It is suggested to use bilinear or bicubic interpolation methods, and not to use nearest neighborhood interpolation method. For each slope surface patch determined by the four neighborhood

DEM grid points, calculate its surface area A_i and projected area B_i on gamma plane; add $A_i \cdot B_i$ to the corresponding pixel in the simulated SAR image. The index of the corresponding pixel can be obtained through SAR geometric correction. Note that shadow detection must be applied before adding the area factor $A_i \cdot B_i$ to the simulated SAR image, surface patches that are in the SAR shadow regions should be excluded from this operation. Detailed methods for calculation of slope surface patches areas and related projected areas and shadow detection are proposed in the following sections.

2.3. Calculation of Slope Surface Areas and Related Projected Areas

As shown in Figures 2(a)–(c), axis x is the azimuth direction; y is the ground range direction; z is the vertical; $\vec{R}$ is the radar line of sight; $\vec{n}$ is the slope surface normal; $\vec{n}_\gamma = -\vec{R}$ is the gamma plane normal. θ is the incidence angle. φ is the angle between the slope surface normal $\vec{n}$ and reference plane normal $\vec{n}_\gamma$, u is the angle between the slope surface normal $\vec{n}$ and vertical z. A is the area of the slope surface patch, B and D are the corresponding projected areas on the gamma plane and the horizontal plane respectively. Those areas can be related by

$$A = \frac{D}{\cos u} \tag{8}$$

$$B = A \cdot |\cos \varphi| \tag{9}$$

Given the DEM sample space δ_x and δ_y along azimuth and ground range direction respectively, $D = \delta_x \cdot \delta_y$. The projection factors $\cos\varphi$, $\cos u$ can be calculated as

$$\cos\varphi = \vec{n} \cdot \vec{n}_\gamma = -\vec{n} \cdot \vec{R} \tag{10}$$

$$\cos u = \vec{n} \cdot \vec{z} \tag{11}$$

where "$\cdot$" denotes scalar product; "$\times$" denotes vector product.

$$\vec{R} = [0 \quad -\sin\theta \quad -\cos\theta]^T \tag{12}$$

$$\vec{z} = [0 \quad 0 \quad 1]^T \tag{13}$$

where "T" denotes transpose of a vector or matrix. As shown in Figure 2(c), for each slope surface patch, the unit vector $\vec{n}$ can be calculated as:

$$\vec{n} = \frac{\vec{v}_x \times \vec{v}_y}{\left|\vec{v}_x \times \vec{v}_y\right|} \tag{14}$$

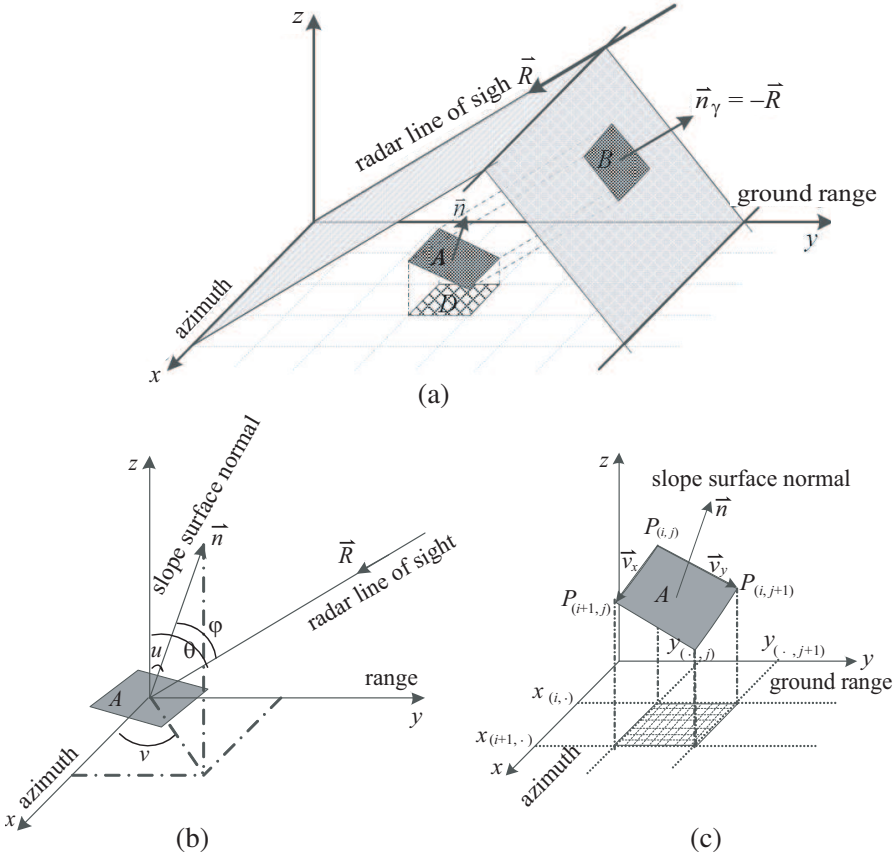

Figure 2. Geometry of slope surface area and related projected area calculation. (a) A slope surface patch and its projection on the gamma plane; (b) Angles between the slope surface normal and related vectors; (c) Calculation of the slope surface normal using DEM data.

For the slope surface patch shown in Figure 2(c)

$$\begin{aligned}\vec{v}_x &= \begin{bmatrix} x_{(i+1,j)} - x_{(i,j)} & y_{(i+1,j)} - y_{(i,j)} & z_{(i+1,j)} - z_{(i,j)} \end{bmatrix}^T \\ &= \begin{bmatrix} \delta_x & 0 & \mathrm{DEM}(i+1,j) - \mathrm{DEM}(i,j) \end{bmatrix}^T \end{aligned} \tag{15}$$

$$\begin{aligned}\vec{v}_y &= \begin{bmatrix} x_{(i,j+1)} - x_{(i,j)} & y_{(i,j+1)} - y_{(i,j)} & z_{(i,j+1)} - z_{(i,j)} \end{bmatrix}^T \\ &= \begin{bmatrix} 0 & \delta_y & \mathrm{DEM}(i,j+1) - \mathrm{DEM}(i,j) \end{bmatrix}^T \end{aligned} \tag{16}$$

For simplicity, we can also represent slope surface normal $\vec{n}$ using

spherical angles u, v as defined in Figure 2(b)

$$\vec{n} = [\sin u \cos v \quad \sin u \sin v \quad \cos u]^T \tag{17}$$

$$\cos\varphi = -\vec{n} \cdot \vec{R} = \sin u \sin v \sin\theta + \cos u \cos\theta \tag{18}$$

2.4. Shadow Detection

Figure 3 shows the formation of shadow regions in SAR imaging geometry. Consider one record line here. Axis y denotes the ground range direction, while z denotes the vertical direction; point P is the position of radar sensor. $y_1, y_2, \ldots, y_N$ are the horizontal coordinates of DEM grid points, while $z_1, z_2, \ldots, z_N$ are the corresponding DEM value. The slope of the topographic curve at point (y_i, z_i) can be calculated as:

$$k_i = \frac{z_{i+1} - z_i}{y_{i+1} - y_i} \tag{19}$$

where $i = 1, 2, \ldots, N-1$.

In ground range direction, these shadow areas can be considered as in several continuous intervals. For example, we consider one continuous shadow region in the interval $[y_m, y_n)$. We call the point (y_n, z_n) as a "turning point" because it is a start of a shadow region interval from right side to left side. For the right end point of the line, i.e., (y_N, z_N), if

$$k_{N-1} \geq \frac{z_P - z_N}{y_P - y_N} \tag{20}$$

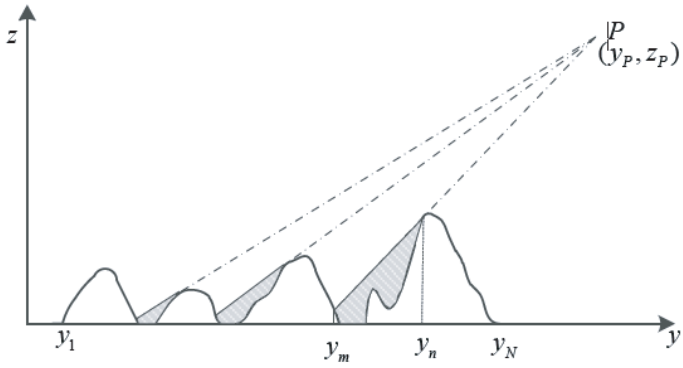

Figure 3. Formation of shadow regions.

(y_N, z_N) is a turning point. For other points (y_n, z_n) $(n = 1, 2, \ldots, N-1)$, if

$$\begin{cases} k_n < \dfrac{z_P - z_n}{y_P - y_n} \\ k_{n-1} \geq \dfrac{z_P - z_n}{y_P - y_n} \end{cases} \tag{21}$$

(y_n, z_n) is a turning point.

All the points (y_i, z_i) in the shadow region interval $[y_m, y_n)$ satisfy

$$\frac{z_P - z_i}{y_P - y_i} \geq \frac{z_P - z_n}{y_P - y_n} \tag{22}$$

Other shadow areas satisfy the same rules. Therefore we can detect the shadow areas from right side to left side using the following method:

i. From near range to far range, i.e., from right side to left side in Figure 3, search for the first turning point that satisfies Equation (20) or (21).

ii. Check if the next point on the left side of current turning point satisfies Equation (22). If Equation (22) is satisfied, mask the point as a shadow point and go to the next point. Iterate this step until Equation (22) is not satisfied, which means the current point is located outside of the shadow area interval.

iii. From right side to left side, search for the next turning point that satisfies Equation (21). Once the next turning point is found, mark it as the current turning point and go to step ii.

Detailed flowchart of the proposed shadow detection method is shown in Figure 4.

2.5. POA Shift Compensation

Polarization angle is one of the parameters that characterize the polarization state of an electromagnetic wave. In sloped areas, the azimuth slope causes shift of POA, thus changes the polarization state of scattered wave, and distorts the analysis of scattering characteristics of the targets. According to [12–14], POA shift η can be calculated using DEM data

$$\tan\eta = \frac{\tan\omega}{-\tan\zeta\cos\theta + \sin\theta} \tag{23}$$

where $\tan\omega$ is the azimuth slope, $\tan\zeta$ is the slope in ground range direction, θ is the incidence angle. And the backscatter matrix S_2 can

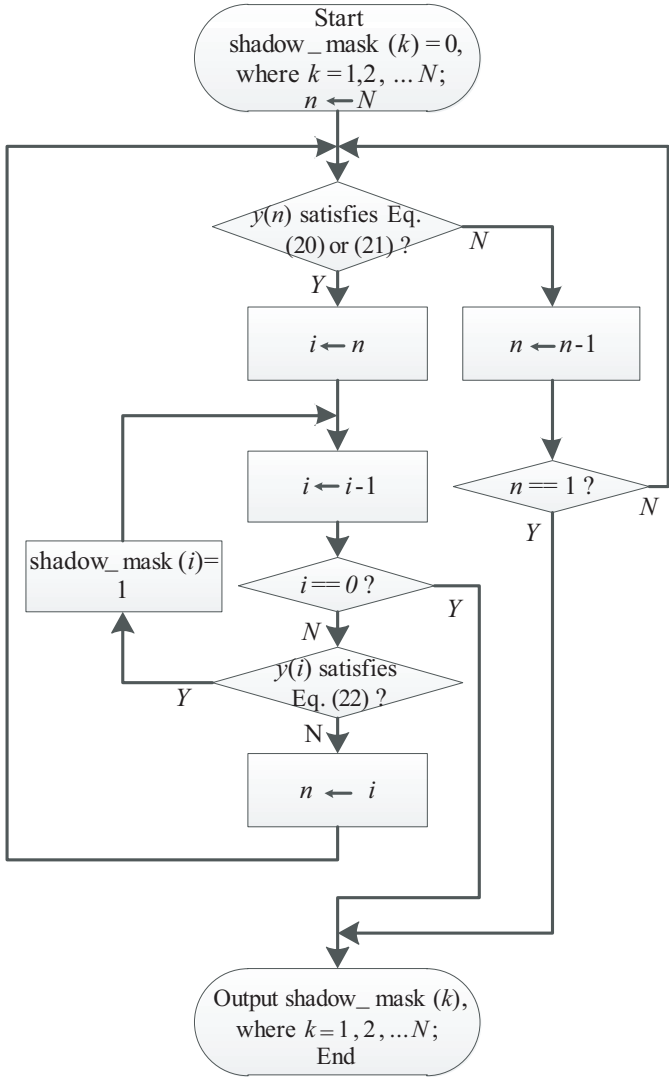

Figure 4. Flow chart for shadow detection.

be corrected using

$$S_2' = \begin{bmatrix} \cos(\eta) & -\sin(\eta) \\ \sin(\eta) & \cos(\eta) \end{bmatrix} \cdot S_2 \cdot \begin{bmatrix} \cos(\eta) & \sin(\eta) \\ -\sin(\eta) & \cos(\eta) \end{bmatrix} \tag{24}$$

2.6. Polarimetric SAR Terrain Correction Procedure

A procedure for polarimetric SAR terrain correction is implemented in our study (as shown in Figure 5), including geometric correction, shadow detection, radiometric correction, and polarization orientation angle compensation.

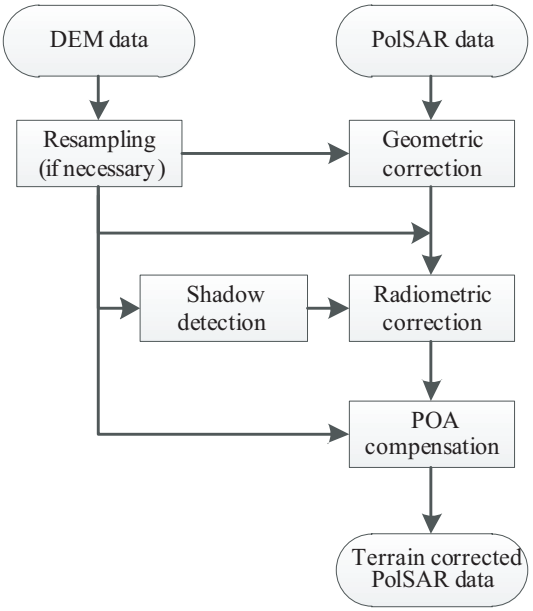

Figure 5. Proposed procedure for terrain effect correction of polarimetric SAR data.

3. EXPERIMENTS

The proposed terrain correction method was applied to a polarimetric Radarsat 2 SAR image to demonstrate the effectiveness of this method. For comparison, two other radiometric correction methods were also implemented in this experiment. One is proposed by Ulander [25], that performs the correction using the angle between the slope surface and the image plane (referred to as URTC for simplicity); the other is proposed by Tilley and Bonwit [26] and Bolter et al. [27], that normalizes the brightness values of SAR image pixels in foreshortening and layover areas by dividing the brightness value equally among all ground patches contributing to that particular SAR pixel (referred to as NRTC for simplicity). Our newly proposed radiometric terrain

correction method is referred to as NewRTC; while the geometric terrain correction is referred to as GTC.

3.1. Study Region and Data Sets

The study region is the Three Gorges Area, located along the Yangtze River in Zigui County, Hubei Province, China. It covers an area of about 1000 km^2. Most part of this region is high relief mountainous areas. The Major LU/LC (land use/land cover) types are built up, bare soil, vegetation, and water.

A RADARSAT-2 C-band Fine Quad polarization SAR image covering this area obtained on November 18, 2010 was used in this study. The incidence angles vary between 22.26° and 24.00° from near range to far range. The pixel size is 4.92 m × 4.73 m (azimuth by slant range).

As a fine spatial resolution DEM was not available, a stereo pair of ASTER (near-infrared) images acquired on September 28, 2003 was used to generate a DEM for the purpose of radar simulation and terrain effect correction. The ASTER images are of 15 m spatial resolution and, with the aid of the 90 m resolution DEM acquired through the Shuttle Radar Topographic Mission and reference information collected by field visits, a revised DEM of 25 m spatial resolution was generated.

A RapidEye satellite image of November 6, 2010 with 5 m spatial resolution covering most part of the study region was also acquired to help with the interpretation of the SAR image.

3.2. Terrain Correction

Firstly, the DEM data was resampled into 2.5 m × 2.5 m pixel size using bilinear interpolation for better accuracy in geometric correction and radiometric correction. Using this resampled DEM data, geometric correction, shadow detection, and radiometric correction was then applied to the RADARSAT-2 data.

Radiometric terrain correction was performed using three different methods URTC, NRTC, and NewRTC after geometric terrain correction (GTC). Together with the geometric corrected data without radiometric correction, four terrain correction methods were applied. For simplicity, they were referred to as "GTC", "GTC + URTC", "GTC + NRTC", and "GTC + NewRTC" respectively. POA shift compensation was then applied to each of those four images. All those four terrain corrected images had the same pixel size of 2.5 m × 2.5 m. The sample space of the original SLC SAR data is 4.9 m in azimuth direction and 11.6 $\sim$ 12.5 m in ground range direction, a 5 × 5 multilook operation was applied to those four terrain corrected images. Boxcar

filter with 5×5 window size was applied to those terrain corrected images to reduce speckle.

3.3. Visual and Quantitative Comparison of the Terrain Corrected Results

Figure 6 shows the Pauli color coded image of those four terrain corrected images. According to Figure 6(a), without radiometric correction, visually, there is remarkable contrast in scattering intensity between front slopes (slopes facing to the radar) and back slopes (slopes facing away from the radar). Those bright white regions on front slopes are with extremely high backscattering intensity caused by small local incidence angle or foreshortening and layover. Figure 6(b) shows that after radiometric correction using URTC,

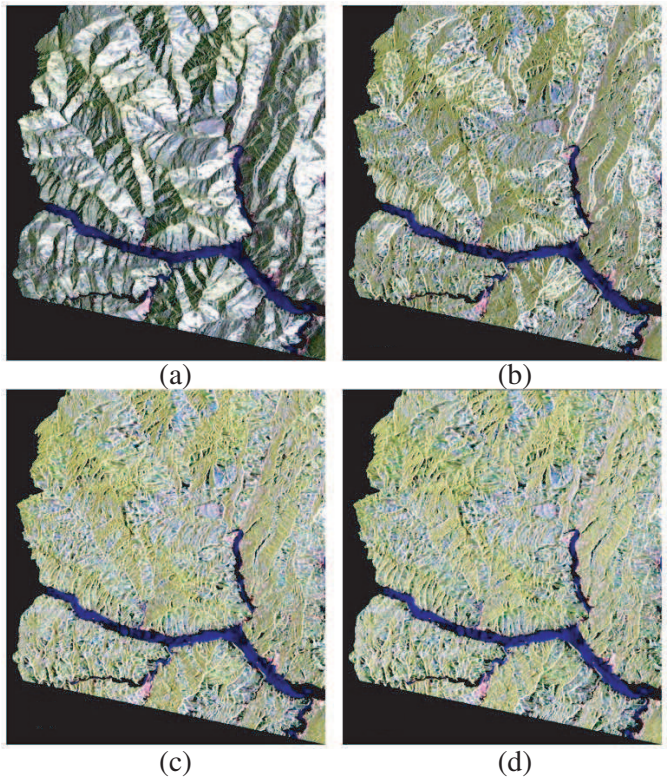

Figure 6. Pauli color coded images after application of different terrain correction methods. (a) GTC; (b) GTC + URTC; (c) GTC + NRTC; (d) GTC + NewRTC.

the contrast between scattering intensity on front slopes and back slopes is reduced, and part of the bright regions on the front slopes disappear. This is because that the scattering intensity difference caused by the local incidence angle difference is reduced. Those bright white regions caused by foreshortening and layover still exist in Figure 6(b), because the slope correction method by Ulander considers only the "one to one" projecting relationship between each DEM sample element and each radar image pixel. Therefore, backscatter values in foreshortening and layover regions cannot be corrected. In Figure 6(c), the contrast between scattering on front slopes and back slopes is reduced furthermore; in fact, most of the bright white regions disappear. Figure 6(d) shows slight improvement compared with (c), with lower contrast between different slopes.

However, there are still some bright lines along the valleys that failed to be corrected. This might because that the special dihedral-like structures in the valleys cause strong SAR response, which cannot be corrected by radiometric correction.

A few of new dark and bright areas appear in the images after radiometric correction in Figures 6(b)–(d). This might be because the bias in geometric correction; thus the radiometric correction factors corresponding to some SAR pixels were incorrectly related. The bias in geometric correction might be caused by the relatively coarse spatial resolution of the original DEM.

To quantitatively investigate the effects of different terrain correction methods, the backscatter values statistics on front slopes and back slopes are calculated. Usually, backscatter value of polarimetric SAR is represented using polarimetric backscattering power *SPAN*

$$SPAN = |S_{HH}|^2 + |S_{HV}|^2 + |S_{VH}|^2 + |S_{VV}|^2 \tag{25}$$

Generally, it is converted into dB form

$$SPAN|_{\mathrm{dB}} = 10 \log_{10} SPAN \tag{26}$$

16 pairs of sample areas were randomly selected on the image. For each pair of sample areas, one is on the front slope, while the other is on the back slope, close to each other. Table 1 displays the mean values of $SPAN|_{\mathrm{dB}}$ of the two areas, the absolute difference values, and average values of the absolute difference values of all the 16 pairs.

As shown in Table 1, without radiometric correction, the average mean value difference between front slopes and back slopes is 12.5 dB; after radiometric correction with different methods, the differences between front slopes and back slopes are all reduced to some extent. The new proposed method performs the best for reducing the backscatter difference to 1.3 dB between different slopes; NRTC

yields a slightly inferior result, 1.8 dB; URTC performs not as good as the other two radiometric correction methods, the average backscatter difference between front slopes and back slopes was reduced to 5.3 dB. This agrees with the visually analysis.

Note that although there is just a 0.5 dB difference between the results of NRTC and NewRTC, there exist inherent reasons. According to the NRTC method, in foreshortening and layover areas where N slope surface patches are projected into one pixel in the SAR image, the brightness value is normalized by dividing it equally into these N patches. However, since the local incidence angles of these N patches might be different from each other, the scattering contribution of each patch to the corresponding SAR image pixel might be different correspondingly. In our NewRTC method, the different local incidence angles were taken into account in the calculation of these N patches' projected area in the gamma plane. Therefore, the correction results of NewRTC approach is expected to be better than that of NRTC in theory.

Table 1. Statistics of backscatter intensity *SPAN* (dB).

	GTC			GTC + URTC		
No.	F	B	$\|F-B\|$	F	B	$\|F-B\|$
1	6.8	−2.6	9.4	3.2	−3.6	6.7
2	11.4	−5.3	16.7	1.7	−6.2	7.9
3	11.6	−3.9	15.6	−3.5	−4.9	1.3
4	5.1	−3.6	8.7	2.3	−5.6	7.9
5	7.8	−3.9	11.7	3.1	−4.7	7.8
6	4.8	−6.7	11.4	2.8	−7.1	10.0
7	9.0	−4.6	13.6	−4.9	−5.2	0.2
8	2.5	−4.6	7.2	1.4	−5.8	7.2
9	6.0	−4.4	10.4	3.9	−5.3	9.2
10	4.9	−3.5	8.3	1.9	−5.1	7.0
11	9.2	−3.3	12.5	−5.9	−5.0	0.9
12	9.3	−1.7	11.0	-5.1	−4.4	0.7
13	12.2	−5.3	17.6	1.6	−6.2	7.8
14	10.5	−6.1	16.6	−4.6	−6.8	2.1
15	9.3	−5.1	14.4	-1.3	−5.7	4.4
16	12.5	−3.3	15.9	−0.7	−4.9	4.1
Mean			12.5			5.3

No.	GTC + NRTC			GTC + NewRTC		
	F	B	$\lvert F-B\rvert$	F	B	$\lvert F-B\rvert$
1	2.7	0.8	1.9	3.4	3.4	0.0
2	1.9	−1.1	2.9	2.5	1.4	1.0
3	−0.8	0.0	0.8	0.0	2.6	2.6
4	1.9	−1.1	3.0	3.0	1.0	2.0
5	1.6	0.1	1.5	2.8	2.8	0.0
6	1.4	−2.3	3.6	2.2	0.6	1.6
7	−1.0	−0.4	0.6	−0.4	2.4	2.8
8	1.2	−0.1	1.2	1.4	2.1	0.7
9	2.8	−0.8	3.6	3.6	1.8	1.8
10	0.4	−0.6	1.0	1.3	1.8	0.5
11	-0.7	−0.2	0.5	0.1	2.0	1.8
12	−1.1	−0.1	1.0	−0.4	1.9	2.3
13	1.8	−1.1	2.9	2.4	1.4	1.0
14	0.1	−1.8	1.8	0.8	0.9	0.1
15	−1.2	−0.9	0.3	−0.3	1.8	2.1
16	1.5	−0.4	1.8	2.1	2.0	0.1
Means			1.8			1.3

Note: F: backscatter intensity from front slope; B: backscatter intensity from back slope; No.: serial number of sample area pairs.

3.4. Application of SAR Terrain Correction to LU/LC Mapping

Supervised Wishart classifier [2] was used to classify the polarimetric SAR data sets after applying different terrain correction methods. In our study region in the Three Gorges Area, China, there are four main land use and land cover (LU/LC) types. They are built-up, bare soil, water, and vegetation. Training samples for those four LU/LC types were carefully selected and interpreted using the polarimetric SAR color coded image, with reference to the RapidEye image, and other optical images on Google Earth. It is observed that pixels with extremely high backscatter values in the image without radiometric correction (shown in Figure 6(a)) are located in seriously foreshortened areas. Pixels with extremely low and high values in the radiometrically corrected images (shown in Figures 6(b)–(d)) might be caused by the incorrectly related radiometric correction factors induced by the bias in geometric correction, as discussed in the last section. These pixels will

interfere with the LU/LC classification results; therefore, we classified them into invalid dark and bright areas. The classification results are shown in Figure 7.

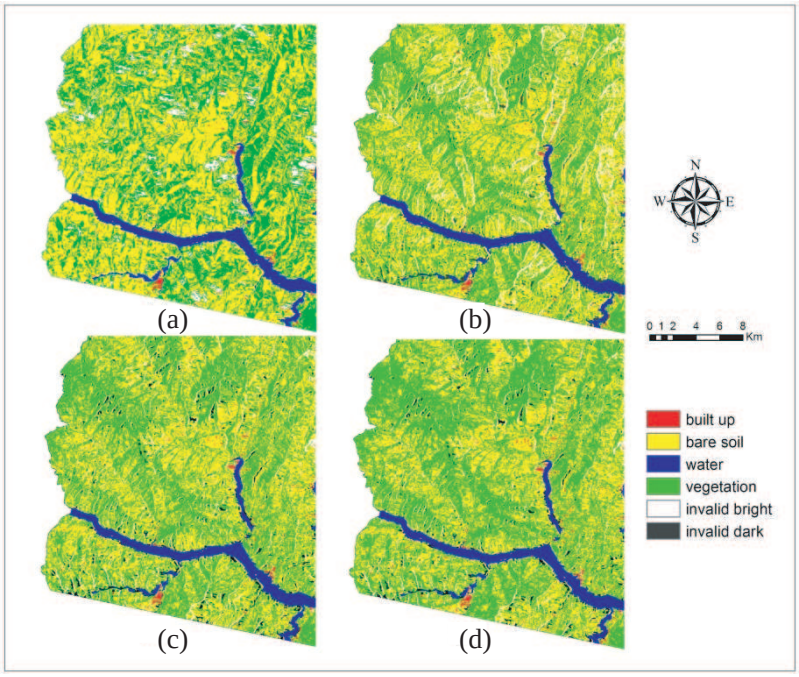

Figure 7. Polarimetric Wishart supervised classification results using four terrain correction methods. (a) GTC; (b) GTC + URTC; (c) GTC + NRTC; (d) GTC + NewRTC.

After the supervised classification, classification results of different terrain correction methods are assessed using a set of independent testing samples. 700 testing samples were randomly generated by PCI Geomatica software, and visually interpreted by referencing to the polarimetric SAR Pauli color coded image, the RapidEye image, and images on Google Earth. Samples with uncertain class labels were excluded from the testing samples. 597 samples were identified as testing samples. Table 2 shows the classification accuracy statistics.

The overall accuracy for the four LU/LC classes was only 57.0% (Kappa = 0.331) without radiometric correction; while by applying our proposed new radiometric terrain correction method, the overall accuracy was improved to 68.2% (Kappa = 0.498). As a comparison, from the overall accuracy, URTC and NRTC perform better than

Table 2. Classification assessment.

	GTC β^0		GTC + URTC σ_U^0	
	producer	user	producer	user
Built up	81.8%	77.1%	63.6%	80.8%
Bare soil	58.1%	57.8%	55.8%	68.0%
Water	75.5%	100.0%	73.5%	97.3%
Vegetation	48.8%	57.1%	65.7%	62.0%
	overall	kappa	overall	kappa
	57.0%	0.331	61.8%	0.408
	GTC + NRTC σ_N^0		GTC + NewRTC σ_T^0	
	producer	user	producer	user
Build up	60.6%	71.4%	69.7%	85.2%
Bare Soil	55.8%	70.3%	56.4%	76.1%
Water	75.5%	100.0%	76.6%	100.0%
Vegetation	70.2%	63.7%	78.9%	65.8%
	overall	kappa	overall	kappa
	63.7%	0.435	68.2%	0.498

without radiometric correction, but less effective compared with our proposed radiometric correction method. This agrees with the visual and quantitative comparison of the terrain corrected results, and again demonstrates the effectiveness of our newly proposed radiometric terrain correction method.

4. CONCLUSION AND DISCUSSION

In this research, a new method for SAR radiometric terrain correction was proposed. The methods for projected area calculation and shadow detection used in radiometric terrain correction were also proposed. Based on these methods, a procedure for polarimetric SAR terrain effect reduction was introduced, including geometric terrain correction, radiometric terrain correction, and polarization orientation angle shift compensation. A RADARSAT-2 polarimetric SAR image over Three Gorges Area, China was used in the experiments to demonstrate the effectiveness of the terrain effect correction method. The visual and quantitative comparisons of images without radiometric correction and with our radiometric correction method indicate that, after applying our proposed radiometric correction, the contrast between the

backscatter values from front slopes and back slopes is reduced. The average difference of polarimetric SAR backscatter intensity from front slopes and back slopes are reduced from 12.5 dB without radiometric correction to 1.3 dB after applying our radiometric correction method. LU/LC classifications using polarimetric SAR images before and after applying radiometric correction indicate that after applying our proposed radiometric correction, the overall accuracy increased by 11.2%. Two other radiometric terrain correction methods were also applied for comparison. One was proposed by Ulander [25]; the other was proposed by Tilley and Bonwit [26] and Bolter et al. [27]. Experiments indicate that our radiometric correction method performs better to reduce the radiometric distortions induced terrain effects.

Although the effectiveness of our proposed polarimetric SAR terrain effect correction was demonstrated by the experiments, it still needs to be improved. In SAR foreshortening and layover areas, we assumed that the ground patches overlapped together have the same backscatter coefficient, however, in fact, there might be different land cover types, thus with different backscatter coefficients; besides, the backscatter coefficients of different land cover types have different variation regulations along with the change of local incidence angle. Problems may also exist for polarization orientation angle shift compensation to these ground patches overlapped together if they have different surface slopes. In this condition, the polarization matrix is a summation of a set of rotated polarization matrix, thus the radiometric distortions and polarization distortions are coupled with each other and cannot be corrected independently. This is an underdetermined problem, thus proper assumption and approximation have to be made to get useful result.

ACKNOWLEDGMENT

This work was supported by an NSERC Discovery Grant awarded to Dr. Wang, the High Technology Research and Development Program of China (2011AA120401), the National Natural Science Foundation of China Key Program (Grant No. 60890071), Program of National Natural Science Foundation for Young Scientists of China (Grant No. 60902100). The RADARSAT-2 polarimetric SAR data was provided by MacDonald Dettwiler and Associates Ltd. (MDA) and Canadian Space Agency (CSA) via the RADARSAT-2 Science and Operational Applications Research (SOAR) program. The software PolSARpro we used to extract RADARSAT-2 data was provided free by European Space Agency (ESA).

REFERENCES

1. Kong, J. A., S. H. Yueh, H. H. Lim, R. T. Shin, and J. J. van Zyl, "Classification of earth terrain using polarimetric synthetic aperture radar images," *Progress In Electromagnetics Research*, Vol. 3, 327–370, 1990.
2. Lee, J. S., et al., "Classification of multi-look polarimetric SAR imagery-based on complex wishart distribution," *International Journal of Remote Sensing*, Vol. 15, 2299–2311, 1994.
3. Lee, J. S., et al., "Unsupervised classification using polarimetric decomposition and the complex Wishart classifier," *IEEE Transactions on Geoscience and Remote Sensing*, Vol. 37, 2249–2258, 1999.
4. Pottier, E. and J. S. Lee, "Application of the 'H/A/(alpha)underba' polarimetric decomposition theorem for unsupervised classification of fully polarimetric SAR data based on the Wishart distribution," *CEOS SAR Workshop*, Vol. 450, 335–340, 2000.
5. Lee, J. S., et al., "Unsupervised terrain classification preserving polarimetric scattering characteristics," *IEEE Transactions on Geoscience and Remote Sensing*, Vol. 42, 722–731, Apr. 2004.
6. Mishra, P., D. Singh, and Y. Yamaguchi, "Land cover classification of palsar images by knowledge based decision tree classifier and supervised classifiers based on SAR observables," *Progress In Electromagnetics Research B*, Vol. 30, 47–70, 2011.
7. Ferro-Famil, L. and E. Pottier, "Dual frequency polarimetric SAR data classification and analysis," *Progress In Electromagnetics Research*, Vol. 31, 247–272, 2001.
8. Yang, J., X. She, and T. Xiong, "Iteration based polarimetric SAR image classification," *PIERS Proceedings*, 47–50, Beijing, China, Mar. 26–30, 2007.
9. Zhang, Y., L. Wu, and G. Wei, "A new classifier for polarimetric SAR images," *Progress In Electromagnetics Research*, Vol. 94, 83–104, 2009.
10. Jin, Y. Q., "Polarimetric scattering modeling and information retrieval of SAR remote sensing — A review of FDU work," *Progress In Electromagnetics Research*, Vol. 104, 333–384, 2010.
11. Lee, J. S. and E. Pottier, *Polarimetric Radar Imaging: Form Basics to Applications*, Taylor & Francis Group, New York, 2009.
12. Lee, J. S., et al., "Polarimetric SAR data compensation for terrain azimuth slope variation," *IEEE Transactions on Geoscience and Remote Sensing*, Vol. 38, 2153–2163, 2000.

13. Lee, J. S., et al., "On the estimation of radar polarization orientation shifts induced by terrain slopes," *IEEE Transactions on Geoscience and Remote Sensing,* Vol. 40, 30–41, Jan. 2002.
14. Lee, J.-S. and T. L. Ainsworth, "The effect of orientation angle compensation on coherency matrix and polarimetric target decompositions," *IEEE Transactions on Geoscience and Remote Sensing,* Vol. 49, 53–64, Jan. 2011.
15. Meier, E., et al. (eds.), "SAR geocoding: Data and systems," *Precise Terrain Corrected Geocoded Images*, Hervert Wichmann Verlag GmbH, Karlsruhe, 1993.
16. Loew, A. and W. Mauser, "Generation of geometrically and radiometrically terrain corrected SAR image products," *Remote Sensing of Environment*, Vol. 106, 337–349, Feb. 15, 2007.
17. Small, D., "Flattening gamma: Radiometric terrain correction for SAR imagery," *IEEE Transactions on Geoscience and Remote Sensing,* Vol. 49, 3081–3093, Aug. 2011.
18. Chen, Z. H. and J. F. Wang, "A new method for minimizing topographic effects on RADARSAT-1 images: An application in mapping human settlements in the mountainous three gorges area, China," *Canadian Journal of Remote Sensing,* Vol. 34, 13–25, Feb. 2008.
19. Guindon, B. and M. Adair, "Analytic formulation of spaceborne SAR image geocoding and 'value-added' product generation procedures using digital elevation data," *Canadian Journal of Remote Sensing,* Vol. 18, 2–12, Jan. 1992.
20. Corner, W. R. and W. G. Rees, *The Simulation of Geometric Distortion in A Synthetic Aperture Radar Image of Alpine Terrain*, 1995.
21. Freeman, A. and J. C. Curlander, "Radiometric correction and calibration of SAR images," *Photogrammetric Engineering and Remote Sensing*, Vol. 55, 1295–1301, Sep. 1989.
22. Holecz, F., et al., "Rigorous derivation of backscattering coefficient," *IEEE Geoscience and Remote Sensing Society Newsletter*, 6–14, 1994.
23. Vanzyl, J. J., et al., "The effect of topography on SAR calibration," *IEEE Transactions on Geoscience and Remote Sensing*, Vol. 31, 1036–1043, 1993.
24. Goering, D. J., et al., "Removal of terrain effects from SAR satellite imagery of arctic tundra," *IEEE Transactions on Geoscience and Remote Sensing*, Vol. 33, 185–194, Jan. 1995.

25. Ulander, L. M. H., "Radiometric slope correction of synthetic-aperture radar images," *IEEE Transactions on Geoscience and Remote Sensing*, Vol. 34, 1115–1122, Sep. 1996.
26. Tilley, D. G. and K. S. Bonwit, "Reduction of layover distortion in SAR imagery," *Remote Sensing of Environment*, Vol. 27, 211–220, Mar. 1989.
27. Bolter, R., et al., "Geocoding in SAR layover areas," *2nd European Conference on Synthetic Aperture Radar*, 481–484, Friedrichshafen, Germany, 1998.
28. Small, D., et al., "Terrain-flattened gamma nought Radarsat-2 backscatter," *Canadian Journal of Remote Sensing,* Vol. 37, 493–499, Oct. 2011.
29. Schuler, D. L., et al., "Compensation of terrain azimuthal slope effects in geophysical parameter studies using polarimetric SAR data," *Remote Sensing of Environment*, Vol. 69, 139–155, Aug. 1999.
30. Yamaguchi, Y., et al., "Four-component scattering power decomposition with rotation of coherency matrix," *IEEE Transactions on Geoscience and Remote Sensing,* Vol. 49, 2251–2258, Jun. 2011.
31. Raney, R. K., et al., *A Plea for Radar Brightness*, 1994.